

1 A study of the Heliocentric dependence of Shock Standoff Distance and Geometry
2 using 2.5D MHD Simulations of CME-driven shocks

3

4 Running Heads: 2.5D Simulated CME shock-sheath distance

5

6

7 N. P. Savani^{1,6†}, D. Shiota², K. Kusano^{3,7}, A. Vourlidas⁴, N. Lugaz⁵

8

9 1. University Corporation for Atmospheric Research (UCAR), Boulder, Co, USA

10 2. Computational Astrophysics Laboratory, Advanced Science Institute, RIKEN, 2-1, Hirosawa, Wako, Saitama
11 351-0198, Japan

12 3. Solar-Terrestrial Environment Laboratory, Nagoya University, Nagoya 464-8601, Japan

13 4. Space Science Division, Naval Research Laboratory, Washington, DC 20375-5352, USA

14 5. Experimental Space Plasma Group, University of New Hampshire, USA

15 6. NASA Goddard space flight center, Maryland, USA

16 7. Japan Agency for Marine-Earth Science and Technology, Yokohama, Kanagawa 236-0001, Japan

17

18 Email: neel.savani02@imperial.ac.uk

19

20 † This work was in part performed during a JSPS fellowship at Nagoya University

21
22
23
24
25
26
27
28
29
30
31
32
33
34
35
36
37
38
39
40
41
42
43
44

Abstract

We perform four numerical magnetohydrodynamic simulations in 2.5 dimensions (2.5D) of fast Coronal Mass Ejections (CMEs) and their associated shock fronts between 10Rs and 300Rs. We investigate the relative change in the shock standoff distance, Δ , as a fraction of the CME radial half-width, D_{ob} (i.e. Δ/D_{ob}). Previous hydrodynamic studies have related the shock standoff distance for Earth's magnetosphere to the density compression ratio ($DR, \rho_u/\rho_d$) measured across the bow shock (Spreiter, Summers, & Alksne 1966). The DR coefficient, k_{dr} , which is the proportionality constant between the relative standoff distance (Δ/D_{ob}) and the compression ratio, was semi-empirically estimated as 1.1. For CMEs, we show that this value varies linearly as a function of heliocentric distance and changes significantly for different radii of curvature of the CME's leading edge. We find that a value of 0.8 ± 0.1 is more appropriate for small heliocentric distances ($<30Rs$) which corresponds to the spherical geometry of a magnetosphere presented by Seiff (1962). As the CME propagates its cross section becomes more oblate and the k_{dr} value increases linearly with heliocentric distance, such that $k_{dr} = 1.1$ is most appropriate at a heliocentric distance of about 80Rs. For terrestrial distances (215Rs) we estimate $k_{dr} = 1.8 \pm 0.3$, which also indicates that the CME cross-sectional structure is generally more oblate than that of Earth's magnetosphere. These alterations to the proportionality coefficients may serve to improve investigations into the estimates of the magnetic field in the corona upstream of a CME as well as the aspect ratio of CMEs as measured in situ.

45 1. Introduction

46
47

48 Although the properties of CMEs have been studied for many years (e.g. Gopalswamy et al. 2009; St Cyr
49 et al. 2000; Vourlidas et al. 2010; Yashiro et al. 2004), it is only recently with the dawn of the STEREO
50 (Eyles et al. 2009; Kaiser et al. 2008) and Coriolis (Eyles et al. 2003; Jackson et al. 2004) missions that
51 their white light structures have been studied much deeper into interplanetary space between the Sun and
52 the Earth (Maloney & Gallagher 2011; Savani et al. 2009). Even then, the white light structures become
53 too dim within the cameras to accurately trace out the global shape as they approach Earth. As such, novel
54 methods to estimate the cross section at terrestrial distances have been investigated. Studies to estimate
55 the cross sectional morphology of CMEs using one dimensional (1D) in situ data have recently been
56 investigated (Russell & Mulligan 2002; Savani et al. 2011b). However these studies not only rely on the
57 properties of the shock front associated to the CME but also assume the geometry and shock standoff
58 distance is identical to Earth's magnetosphere. By using physical arguments, a study by Siscoe and
59 Odstrcil (2008) suggest that this may not be the case. In this paper we test the validity of assuming a
60 magnetosheath as an appropriate geometry for a sheath region ahead of a CME.

61

62 CMEs observed remotely from coronagraphs after they are initially launched off the Sun are often treated
63 as objects with circular cross-sections (Howard et al. 1982; Krall et al. 2001; Vourlidas, et al. 2010). This
64 circular shape is consistent with theoretical derivations of twisted magnetic field lines that form flux rope
65 structures (Chen 1989; Chen et al. 1997; Titov & Demoulin 1999), which are also used to initiate CMEs
66 in computational models (Lugaz, Manchester, & Gombosi 2005; Manchester et al. 2004; Shiota et al.
67 2005; Shiota et al. 2010). These circular structures (i.e. aspect ratio of 1) found in force-free conditions
68 are often considered to be a correct 'zeroth' order approximation for a class of ICME known as magnetic
69 clouds, which are observed in situ to have a smooth field line rotation consistent with a flux rope. Some
70 of the earliest modelling of in situ data assumed circular cross sections (Burlaga 1988; Lepping, Jones, &
71 Burlaga 1990), and this geometry currently remains as the zeroth order approximation for estimates of
72 their total magnetic flux content at terrestrial distances when considering long term space climate
73 variability and potential space weather effects (Lockwood et al. 2004; Owens & Crooker 2006). However,
74 as a CME propagates at a near constant radial velocity while expanding in the meridional direction to
75 maintain a near-constant angular width, it has long been suspected that a CME could flatten into an
76 elliptical cross-section as it travels further into the heliosphere (Riley & Crooker 2004; Savani et al.
77 2011a). As such, numerous attempts have been made to modify the static picture of a simple constant- α

78 flux rope fitting (Hidalgo et al. 2002; Marubashi 1986; Mulligan & Russell 2001; Owens, Merkin, &
79 Riley 2006).

80

81 Russell and Mulligan (2002) suggested that the aspect ratio of a CME may be estimated from measuring
82 the distance between the shock and the leading edge of the CME (shock standoff distance, Δ) and then by
83 assuming that the geometry of Earth's bow shock is appropriate for interplanetary CMEs (ICMEs; see
84 figure 1). The authors therefore began the derivation of their estimates from the semi-empirical formula
85 (Spreiter, et al. 1966),

86

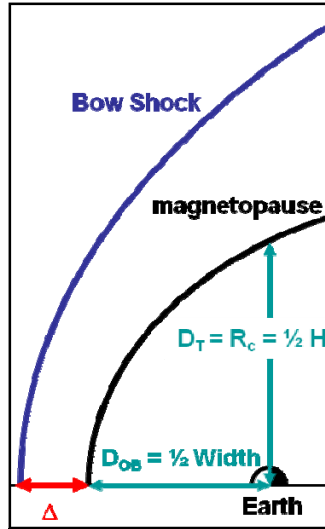
$$87 \quad \frac{\Delta}{D_{OB}} = 1.1 \frac{\rho_u}{\rho_d} \quad (1)$$

88

89 which is based on gas-dynamic theory for Earth's magnetosphere, where D_{OB} is the distance from the
90 center to the nose of the obstacle (originally the Earth's magnetopause), ρ is the plasma density and the
91 subscripts 'u' and 'd' denote up and downstream of the shock, respectively. D_{OB} was then later substituted
92 for the vertical extent of the obstacle (D_T , see section 2 for details). The density compression ratio (DR)
93 coefficient, $k_{dr}=1.1$ was calculated experimentally under laboratory conditions. A metallic object, oblate
94 in shape, was fired through neutral argon gas and snapshots in time were taken during its propagation.
95 This allowed measurements to be taken for the shape and location of the shock front in relation to the
96 obstacle under different firing speeds, which correlate to the compression of gas across the shock front.
97 As much of the theory that correlates this sheath geometry to a CME is fundamentally based on this
98 empirical equation in this paper (see section 2 for details), we investigate the robustness of k_{dr} for fast
99 CMEs travelling between the Sun and 1AU.

100

101



102

103 Figure 1. Schematic displaying the relationship between Earth's bow shock and characteristics of an
 104 ICME. We relate the width of a CME measured with in situ instruments and the distance from the Earth
 105 to the magnetopause nose (D_{OB}), and the vertical size ($1/2 H$) to the radius of curvature (R_c). (Taken from
 106 Savani, et al. 2011b).

107

108

109 Russell and Mulligan (2002) investigated a CME event from Pioneer Venus Orbiter (PVO) during the
 110 spacecraft's transit to Venus. The authors used in situ data to measure the shock standoff distance, Δ , and
 111 related it to equation 1 in order to predict the aspect ratio of the CME's cross section. The authors
 112 estimated an aspect ratio of 4, which is in agreement to the geometrical prediction by Savani, et al.
 113 (2011a). However, a more thorough investigation of this mathematical formulism by Savani, et al.
 114 (2011b) for 45 events between the ~ 0.5 and 5.5 AU found an average aspect ratio of 2.8 ± 0.5 . From these
 115 results, Savani, et al. (2011b) concluded that deformations to the leading edge of CMEs may occur
 116 frequently, thereby predicting a smaller radius of curvature. But the authors noted that the estimates are
 117 predicted on the assumption that the behaviour of the sheath is identical for interplanetary CMEs and
 118 Earth's magnetosheath. This disparity was highlighted on physical grounds by Siscoe and Odstrcil (2008).
 119 They argued that the transient nature of CMEs and their lateral expansion changes the sheath behaviour
 120 by prohibiting the solar wind from deflecting around the CME. The authors suggest that the solar wind
 121 plasma 'piles up' ahead of the CME, thereby categorising this as an 'expansion sheath' apposed to the
 122 'propagation sheath' for common magnetospheres. Therefore these authors would predict that the
 123 coefficient, k_{dr} would not necessarily equal 1.1 and it may perhaps vary as the CME becomes more
 124 elliptical (i.e. for larger heliocentric distances).

125

126 Analysis based on similar theoretical geometry of equation 1 and detailed in section 2 have been
127 investigated beyond the heliocentric range of Savani, et al. (2011b). Lynnyk et al. (2011) investigated the
128 radius of curvature of CMEs in a similar manner to Russell and Mulligan (2002) and Savani, et al.
129 (2011b), however they concentrated on CMEs detected by the Voyager mission (Burlaga et al. 1981) at
130 much larger heliocentric distances (1 – 30AU).

131

132 Also, the CME geometry based on equation 1, formed the foundation for deducing the magnetic field
133 strength upstream of the CME-driven shock in the solar corona between 1.5 – 23 solar radii (Gopalswamy
134 & Yashiro 2011). In this scenario, the shape of the CME and sheath distance was measured remotely off
135 the limb of the Sun, allowing an estimate of the sound speed Mach number to be made. With further
136 assumptions, an estimate of the magnetic field strength was made.

137

138 Therefore, it is for the reason of multiple research interests, all based on a single semi-empirical formula
139 (equation 1), which has itself been considered questionable, that we investigate the suitability of $k_{dr} = 1.1$.
140 We carry out our investigation with the aid of 2.5D MHD simulations detailed in section 3.

141

142

143 2. Theory

144

145 Spreiter et al. (1966) measured the densities up and downstream as well as the position of the bow shock
146 from an experimental procedure designed to mimic the terrestrial magnetosphere with the aid of an oblate
147 metallic obstacle fired through argon gas. They concluded that $k_{dr} = 1.1$ remains robust for a variety of
148 upstream solar wind velocities (Mach number, M , between 5 and 100) and the ratio of specific heats
149 (polytropic index), γ between 1.1 and 2.

150

151 However, the shape of the obstacle was shown to make a significant impact. Seiff (1962) performed a
152 similar analysis for a spherical obstacle and produced the relation,

153

$$154 \quad \frac{\Delta}{D_{OB}} = 0.78 \frac{\rho_u}{\rho_d} . \quad (2)$$

155

156 The practical application of equations 1 and 2 is carried out by exchanging the ratio of densities to Mach
 157 number. This can be done under hydrodynamic (HD) conditions by invoking the conservation of mass, to
 158 produce the nontrivial solution (Priest 1984)

$$159 \quad \frac{\rho_u}{\rho_d} = \frac{(\gamma-1)M_u^2+2}{(\gamma+1)M_u^2} , \quad (3)$$

160
 161 in terms of the sonic Mach number $M_u \equiv v_u/c_{s,u}$, where $c_{s,u} \equiv (\gamma p_u/\rho_u)^{1/2}$. Here, p is the pressure and
 162 v is the velocity. However, under the more sophisticated magneto-hydrodynamic (MHD) regime,
 163 equation 3 is only applicable for a parallel shock where the velocity and magnetic field are both parallel.
 164 While the MHD solution for a perpendicular shock where the velocity is normal to the shock front
 165 follows (Priest & Forbes 2007):

$$166 \quad 2(2-\gamma) \mathbf{X}^2 + [2\gamma\beta + (\gamma-1)\gamma\beta M_u^2 + 2\gamma] \mathbf{X} - \gamma(\gamma+1)\beta M_u^2 = 0 , \quad (4)$$

167
 168 where $\mathbf{X} = \rho_d/\rho_u$ and β is the upstream plasma beta. Equation 4 is a quadratic equation that can be
 169 solved as a function of Mach number, with the magnetic field serving to reduce \mathbf{X} below its
 170 hydrodynamic value. However for the purposes of CME-driven shocks, current studies have focused on
 171 the application of only the HD case from equation 3. Unfortunately under a low Mach number regime
 172 ($M \lesssim 3$) neither equation 1, 2 nor 3 are valid. This led Farris and Russell (1994) to make an adjustment to
 173 the denominator of equation 3 from $(\gamma+1)M_u^2 \rightarrow (\gamma+1)(M_u^2-1)$. This was done on an intuitive
 174 basis.
 175

176
 177 Even though the Mach number is the observationally measured estimate used to infer the CME-driven
 178 shock properties, we choose to focus on quantifying k_{dr} in the work presented here because the inferred
 179 answers assume the less accurate HD scenario.

180
 181 Farris and Russell (1994) noted that the radius of curvature at the nose of Earth's magnetopause can be
 182 estimated as equal to the vertical extent of a magnetosphere (sometimes called the terminator distance).
 183 Under this assumption the distance from the center of the Earth to the nose of the magnetopause can be
 184 used to estimate the radius of curvature:

$$185 \quad \frac{R_c}{D_{OB}} = 1.35 . \quad (5)$$

186 While, in fact the radius of curvature stated by Spreiter, et al. (1966) is, $R_c = D_{OB}(3 + \sqrt{21})/6$, and is
 187 approximately 1.26 (Verigin et al. 2003).

188
 189 By combining equations 1, 3 and 5 (i.e. under the HD regime) we are able to relate the radius of curvature
 190 of an obstacle based on an oblate magnetosphere to two measurable quantities,

$$191 \quad \frac{\Delta}{R_c} = 0.81 \frac{(\gamma-1)M_u^2+2}{(\gamma+1)M_u^2} ,$$

$$192 \quad \text{for } \gamma = 5/3 \Rightarrow \frac{\Delta}{R_c} = 0.204 + 0.611 M_u^{-2} . \quad (6)$$

193 However, the radius of curvature may be related to the spherical geometry found in equation 2 to produce
 194 the formulae used by Russell and Mulligan (2002):

$$195 \quad \frac{\Delta}{R_c} = 0.58 \frac{(\gamma-1)M_u^2+2}{(\gamma+1)M_u^2} ,$$

$$196 \quad \text{for } \gamma = 5/3 \Rightarrow \frac{\Delta}{R_c} = 0.195 + 0.585 M_u^{-2} . \quad (7)$$

197 The authors performed the calculations with an assumed polytropic index of 5/3. The spherical geometry
 198 inherent in equation 7 is perhaps more applicable than equation 6 for CMEs early in their propagation
 199 phase, when the CME morphology may be considered to have a more idealised circular cross-section. At
 200 a heliocentric distance of $\sim 1.4R_s$, Gopalswamy et al. (2012) showed that the coronal magnetic field can
 201 be indirectly estimated by fitting a circular shape to a CME observed in SDO and by implementing
 202 equation 6. However this analysis required a further assumption that the Alfvén Mach number (M_A) can
 203 be substituted for the gasdynamic sonic Mach number (M), which is a good approximation only for low
 204 Mach numbers in the solar wind (Fairfield et al. 2001).

205
 206

207 3. Numerical Model

208 3.1 Numerical Scheme

209
 210 The axisymmetric simulation performed in this work solves the MHD equations using a finite volume
 211 method with the Harten-Lax-van Leer Discontinuities (HLLD) nonlinear Riemann solver (Miyoshi &
 212 Kusano 2005), the third-order TVD Monotone Upstream-centered Schemes for Conservation Laws
 213 (MUSCL), and the second order Runge-Kutta time integration. Details of the numerical model are
 214 specified in Shiota et al. (2008). The MHD equations implemented in the system follow the equation of
 215 continuity, the equation of motion, the induction equation, and equation of energy with gravity.

216

217 However, this simulation alone without any corrections may violate the divergence-free condition of the
218 magnetic field. As the magnetic field is derived from the solenoidal condition, the simulation may
219 breakdown if the numerical value of $\nabla \cdot \mathbf{B}$ is not sufficiently small. This is corrected in our simulation by
220 employing the hyperbolic divergence B diffusion method (Dedner et al. 2002) and detailed in Shiota, et
221 al. (2008). In essence, once a finite value of $\nabla \cdot \mathbf{B}$ is locally formed within the numerical domain, the
222 quantity is distributed across the full domain and thereby reduces any localised magnitude.

223

224 The numerical domain is axisymmetric in the meridional plane and extends in the radial direction
225 between 4 Rs and 304 Rs. The domain is discretized to a grid of $(nr, n\theta)=(1604,512)$ in a non-uniform
226 manner in order to enhance the resolution at smaller heliocentric distances (Shiota, et al. 2008). The inner
227 boundary is set outside the sonic point at 4 Rs. The thermodynamic effects such as initial coronal heating,
228 radiative cooling and initial acceleration processes for the solar wind are neglected in this study. The
229 electric resistivity is set to be zero, thus causing magnetic reconnection to occur only as a result of
230 numerical diffusion.

231

232

233 3.2 Solar wind

234

235 To obtain the initial steady-state solar wind solutions, we begin with reasonable initial conditions and
236 integrate the MHD equations (Shiota, et al. 2008) in a Cartesian coordinate system while the grid system
237 remains in a spherical system. Initially, a supersonic solar wind is set to be at a uniform speed of
238 300km/s, with a uniform density of $6.33 \times 10^3 \text{ cm}^{-3}$ and at a uniform temperature of $1.32 \times 10^6 \text{ K}$. The initial
239 magnetic field of the Sun is considered to have a simple dipolar configuration. However, as the inner
240 boundary can be considered to be past the source surface (which is usually set at $\sim 2.5R_s$), we assume all
241 the field lines are ‘open’ and directed radially from the Sun. The field direction is flipped at the equator
242 and follows

$$243 \quad \mathbf{B}(X, Z) = B_r(X, Z) \mathbf{e}_r = \frac{B_{r0}}{r^2} \tanh\left(\frac{1}{w_{cs}} \frac{Z}{r}\right) . \quad (8)$$

244 Where $r = \sqrt{X^2 + Z^2}$, $B_{r0} = 3 \text{ G}$, and the current sheet thickness is defined by $w_{cs} = 0.05$. Therefore a field
245 strength of 0.1875 Gauss is injected at the inner boundaries of the poles.

246

247 The specific heat ratio, γ is set to 1.4 in order to simply introduce a small energy source. The heat ratio is
248 set slightly below the average estimate for the solar wind ($\gamma=1.46$) as measured in situ (Kartalev et al.

249 2006; Totten, Freeman, & Arya 1995). As the work presented below investigates the DR coefficient, k_{dr}
250 as defined in equation 1, and the maximum theoretical density compression ratio is intimately linked to γ
251 (i.e. a maximum ratio of 4 when $\gamma=5/3$), it is important for this study to estimate the compressibility of
252 the solar wind appropriately. Many MHD simulations use a reduced non-adiabatic polytropic index of
253 $\gamma=1.05$ as a simplified correction for neglecting the thermodynamic effects in the corona (e.g. Linker et al.
254 1999), however this is not appropriate for our study, therefore we must start our simulation domain above
255 these effects (Pomoell & Vainio 2012). For this reason we set the inner boundary of our domain at 4Rs
256 and fix the initial CME flux rope at 10Rs (see section 3.3 for details on flux rope initiation). It is worth
257 noting that Pomoell, Vainio, and kissmann (2011) studied the dynamics of shocks by setting the heating
258 source term to an appropriate value, such that the polytropic index may be maintain at 5/3 while retaining
259 an identical background solar wind solution produced by a polytropic index of 1.05.

260
261 We also note that 2.5D simulations have been shown to provide comparable results to their 3D equivalent
262 if their initial momentum are identical (Jacobs, van der Holst, & Poedts 2007). Jacobs, et al. (2007)
263 showed that the position of the front and center of mass were comparable to their 3D equivalent. They
264 predicted that the 2.5D simulation would be subject to a smaller drag force because the CME surface is
265 spread over a larger area when compared to the 3D case. Because the domain of the authors work was
266 limited to a maximum heliocentric distance of 30Rs, they predicted the consequence of the smaller drag
267 force would result in an earlier arrival time of the CME at Earth. However their simulation is based on a
268 ‘density-driven’ model which involves the launching of a high-density plasma blob, and therefore does
269 not consider the magnetic forces.

270
271 Our solar wind model has similar parameters to the study performed by Tsurutani et al. (2003); these
272 authors investigated the propagation of a CME-driven shock. Both models are axisymmetric and neither
273 include a bimodal wind nor a spiral interplanetary magnetic field. However Tsurutani, et al. (2003)
274 investigated a spatial regime starting at the solar surface, as such they chose to vary the polytropic index
275 with radial distance in order to accommodate the additional heating source processes occurring in the
276 solar corona. Manchester et al. (2005) compared their findings from a global 3D model with a Gibson-
277 Low magnetic flux rope with that of Tsurutani and co-authors, and found a similar pattern for the shock
278 normal direction at low latitudes. The shock Mach number is found to increase to about 18Rs, whereas
279 Tsurutani, et al. (2003) find that the Mach number approaches a maximum at 130Rs.

280

281

282

283 3.3 CME creation

284

285 As we are interested in the morphology of the CME and the shock position, we do not consider the trigger
 286 process or possible instability conditions for the launch of CMEs (e.g. Antiochos, DeVore, & Klimchuk
 287 1999; Chen & Shibata 2000; Forbes & Priest 1995; Inoue & Kusano 2006; Kusano et al. 2004; Rousev,
 288 Lugaz, & Sokolov 2007). We artificially superimpose a toroidal flux rope onto the background solar wind
 289 as a non-equilibrium structure. The magnetic field inside the flux rope is defined as

290

$$291 \quad \mathbf{B} = \alpha \nabla \times (\Phi \mathbf{e}_\phi) + \nabla \times \nabla \times (\Phi \mathbf{e}_\phi) \quad , \quad (9)$$

292

293 Where \mathbf{e}_ϕ is the unit vector in the ϕ direction, α is the force free parameter and Φ is the flux function. The
 294 magnetic field is semi-analytically calculated by the axisymmetric Grad-Shafranov equation,

295

$$296 \quad \frac{\partial^2 \psi}{\partial X^2} + \frac{\partial^2 \psi}{\partial Z^2} + \left(\frac{1}{4X^2} + \alpha^2 \right) \psi = 0 \quad (10)$$

297

298 where $\psi = \sqrt{X} \Phi$ (similar to the toroidal solution by Miller & Turner 1981) and by applying a boundary
 299 condition of

300

$$301 \quad \Phi = 0 \quad \text{when} \quad r = \sqrt{(X - X_c)^2 + Z^2} \geq a_c \quad . \quad (11)$$

302

303 The variables X_c is the initial heliocentric distance of the flux rope center; a_c is the minor radius of the
 304 flux rope; and $\alpha = 1/X_c$. The Grad-Shafranov equation is solved numerically using the successive over-
 305 relaxation (SOR) method (Press, et al. 1992) by following,

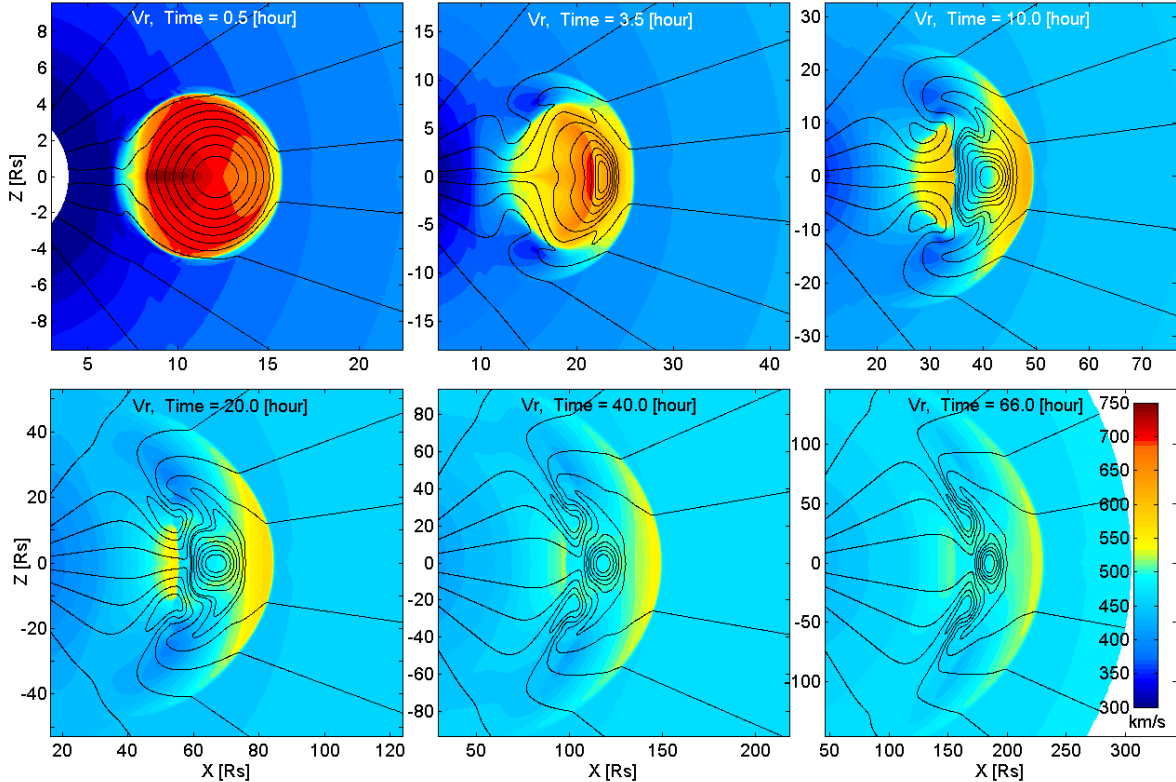
306

$$307 \quad \psi_{i,j}^{n+1} = \psi_{i,j}^n + \omega \left[\frac{\psi_{i+1,j}^n + \psi_{i-1,j}^n}{D \Delta X^2} + \frac{\psi_{i,j+1}^n + \psi_{i,j-1}^n}{D \Delta Z^2} - \psi_{i,j}^n \right] \quad (12)$$

$$D = \left[\frac{1}{4X^2} - \frac{2}{\Delta X^2} - \frac{2}{\Delta Z^2} + \alpha^2 \right].$$

308

309 Where ω , set to equal 1.5, is the extrapolation factor chosen to accelerate the rate of convergence of the
 310 iterates to the solution. The initial plasma density of the flux rope is also defined as twice the surrounding
 311 solar wind value. The magnetic flux threading through the cross-section, $F_L = \iint \mathbf{B}_\phi \, dX \, dZ$. Everywhere
 312 within the flux rope is set to an approximately force-free condition in the initial state. The values of the
 313 parameters investigated in the paper are displayed in table 1.



315
 316 Figure 2. 2.5D simulated flux rope for case study 1 is displayed at six frames during its propagation from
 317 10Rs to ~200Rs. The radial component of the velocity is shown in color within the simulated domain
 318 (between 4Rs and 304Rs). The color bar is the same for all the panels of each of the parameters. The
 319 black curves follow the contours of constant flux function, which trace out the magnetic field lines. Note
 320 that the magnetic field lines in each panel are different to each other.

321
 322

4. Results

323
 324

325 In this paper we use four simulated case-study events to investigate the impact of varying the initial speed
 326 and the size of the flux rope. Case 1 is our benchmark event that begins at 10Rs and has a radial width of
 327 4Rs; see figure 2. This size was chosen by the restrictions imposed by the assumptions used in the
 328 simulation and observational evidence. A restriction to the minimum heliocentric distance for the FR is
 329 set from the inability to correctly consider the effects of coronal heating and the angular width of
 330 approximately 50 degrees is estimated as a typical width of a CME from remote sensing observations (St
 331 Cyr, et al. 2000). The magnetic flux contained within the FR was set to $3 \times 10^{21} \text{Mx}$ which is of a typical
 332 order of magnitude for observed in situ measurements (Kataoka et al. 2009). The magnetic field
 333 magnitudes at Earth for these events are ~90nT which would correspond to very large geo-effective
 334 events (Manchester et al. 2006). The FR is launched with a uniform radial velocity of 700km/s. The other

335 events vary these parameters as shown in table 1. Because our simulation is limited to introducing a FR
 336 with an instantaneous speed rather than with a more gradual acceleration, we are limited to a maximum
 337 initial speed of about 1200km/s (Case 4). Any further increase in speed is found to build up an excess in
 338 magnetic pressure early in the propagation of the FR such that it equilibrates by generating an unusually
 339 large radial expansion. Although this limitation prevents our current study from investigating extreme
 340 events such as the Carrington storm, it does allow us to investigate the more frequently observed fast
 341 CMEs.

342

	Initial Heliocentric, X_c distance, R_s	FR radial Width, a_c R_s	Initial Velocity km/s	Magnetic Flux, F_L Mx
Case 1	10	4	700	3×10^{21}
Case 2	10	2	700	3×10^{21}
Case 3	10	4	900	3×10^{21}
Case 4	10	4	1200	3×10^{21}

343

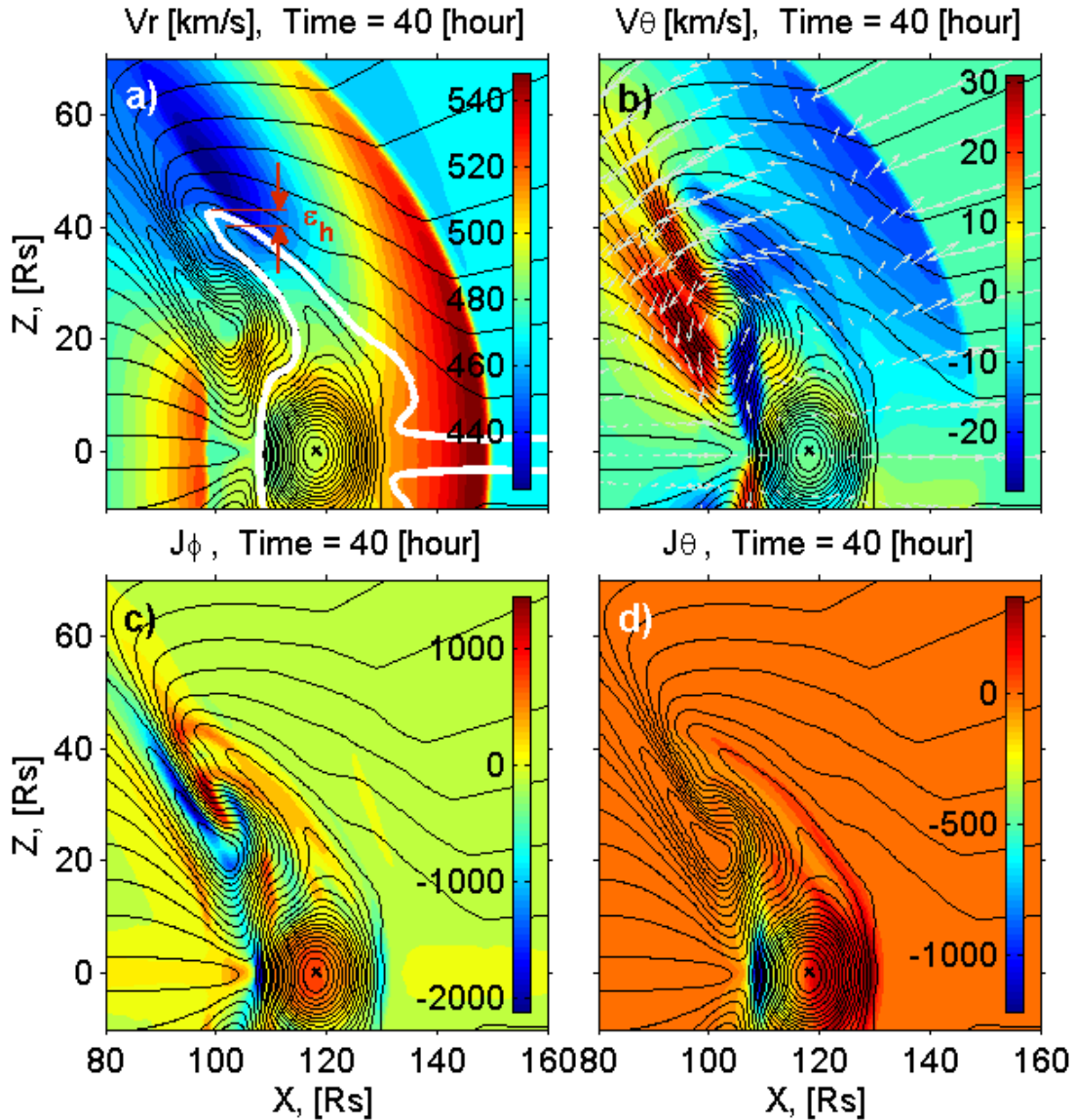
344 Table 1. Initial conditions for the four 2.5D simulated CME case study events.

345

346

347 Figure 3 shows an exploded view of the CME from case 1. Figure 3a displays an extra contour following
 348 the flux function as a white line. This line is manually selected between the open and closed field lines
 349 from the automated contours levels shown in black. The distance between two adjacent open/closed field
 350 lines is then used to estimate the error in the vertical extent (ϵ_n) of the FR. This process was carried out
 351 for each frame that was investigated in further detail. Figure 3b displays the velocity vectors of the solar
 352 wind relative to the center of the flux rope. The theta direction of the spherical coordinate system used in
 353 these simulations is the co-latitude values (i.e. theta increases from the ecliptic north towards the ecliptic
 354 plane). The plasma within the sheath is deflected and slowed down by the leading shock front. Figure 3a
 355 and 3b clearly show the shock boundary, while 3b displays the solar wind smoothly deflecting around the
 356 FR obstacle. Figure 3c and 3d displays the phi and theta components of the current density, J . The change
 357 in the current density emphasizes the approximate location of the FR leading edge.

358

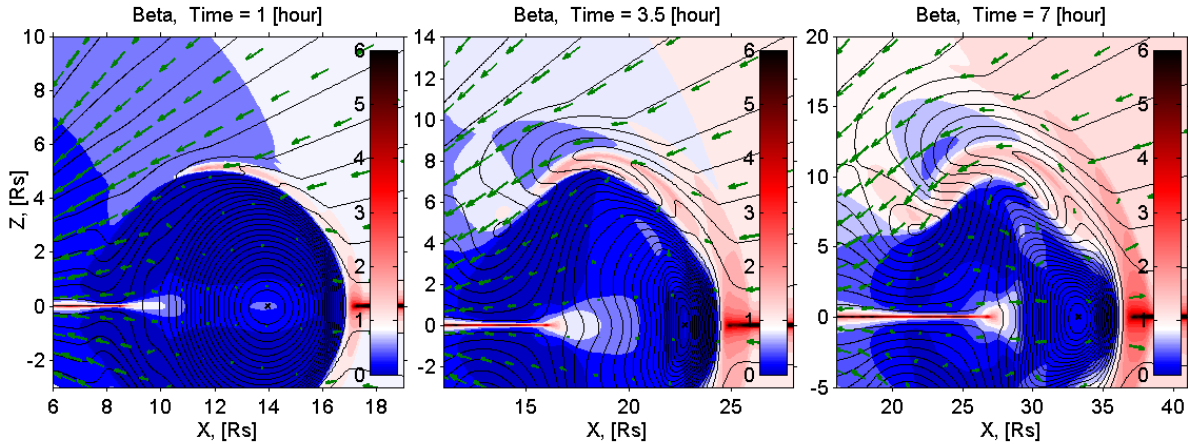


359

360 Figure 3. Displays a 2.5D simulated flux rope for case study 1 at a single time. The variables of the
 361 velocity in the radial and theta direction are displayed in panel a and b, respectively. The current densities
 362 in the phi and theta directions are shown in panels c and d, respectively. The black contours represent
 363 lines of constant flux function, A_ϕ which trace out the magnetic field lines. The white curve in panel a
 364 displays an additional line of constant A_ϕ which is manually selected and used to estimate the error in the
 365 flux rope height as determined by a boundary of closed/open magnetic field lines. Panel b displays vector
 366 arrows in white which display the flow direction of the solar wind referenced from the center of the flux
 367 rope.
 368

369 The plasma beta within the FR for the simulations is below one; the solar wind has a beta value of
 370 approximately one and a higher value is present around the location of the current sheet. These results can
 371 be seen in figure 4. Figure 4 shows three frames during the early propagation phase of the simulated CME
 372 from case 1. The first frame displays a higher beta plasma surrounding the FR leading edge with the

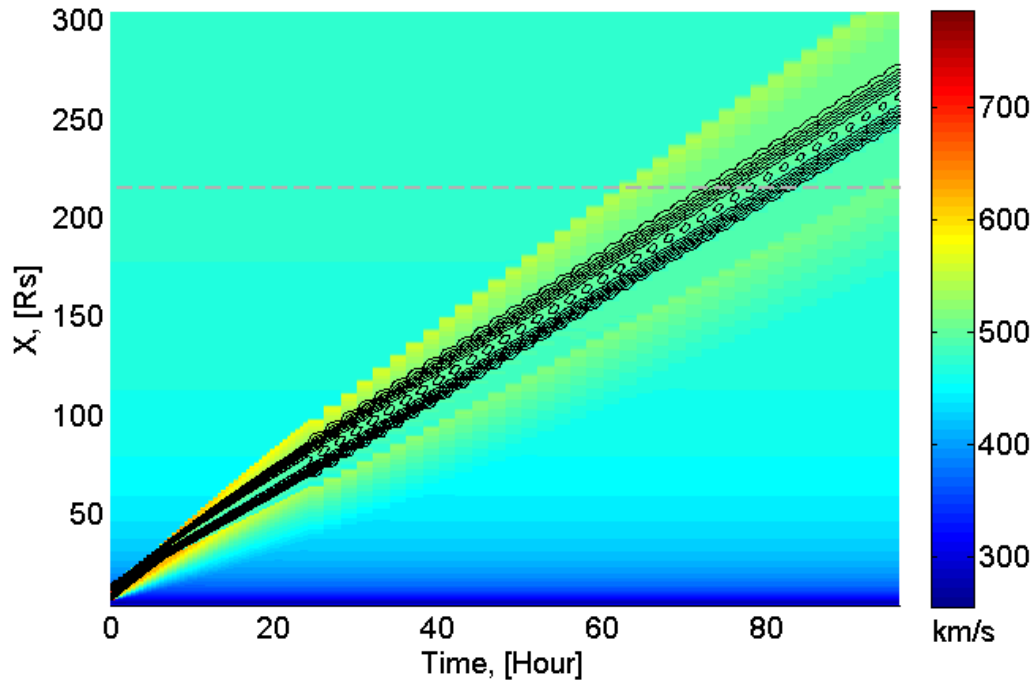
373 leading shock front having recently been formed. The higher beta value within the sheath is indicated by
 374 the red coloration and the plasma smoothly flows around the CME leading edge (green vectors). The
 375 higher beta emphasises the relative importance of the plasma forces above the magnetic forces. The
 376 sheath plasma flows over the CME to the rear side where it interacts with plasma that is more dominated
 377 by the magnetic forces (beta less than one). The latter two frames show the high beta plasma flowing
 378 behind the FR and thus ‘kinking’ the field lines in a manner that forms a flux tube from numerical
 379 diffusion.



380
 381 Figure 4. Displays the plasma beta for the case 1 simulated FR at 3 time frames after its injection into the
 382 solar wind: 1 hour, 3.5 hours and 7 hours. The black lines represent the magnetic field lines and the green
 383 vectors show the plasma flow vectors in relation to the motion of the FR center.

384
 385
 386 As the FR propagates, the shock front spans over a larger position angle, thereby disturbing the solar wind
 387 further north and south than the flux rope itself. However, the location of the shock front and the time
 388 evolution of the shock standoff distance are better viewed as a height-time map, shown in figure 5. The
 389 height-time maps have often been used for locating the heliocentric position of a CME from remote
 390 observations (Sheeley et al. 1999), and have more recently been used to determine their propagation
 391 direction (e.g. Davies et al. 2009; Rouillard et al. 2009). Figure 5 displays the magnetic field contours of
 392 the flux rope as black lines, while the color scale displays the radial velocity. The shock front is clearly
 393 located ahead of the FR and shown as a distinct boundary on the color scale. Behind the rear edge of the
 394 FR shows a region where the solar wind velocity changes rapidly.

395
 396



397

398 Figure 5. Height-Time map of the flux rope along the ecliptic plane. The color scale displays the radial
 399 component of the velocity and the black contours are the same field lines of the flux rope as displayed in
 400 figure 2. The grey dashed line is at a constant heliocentric of 215 Rs, indicating the location of Earth.
 401

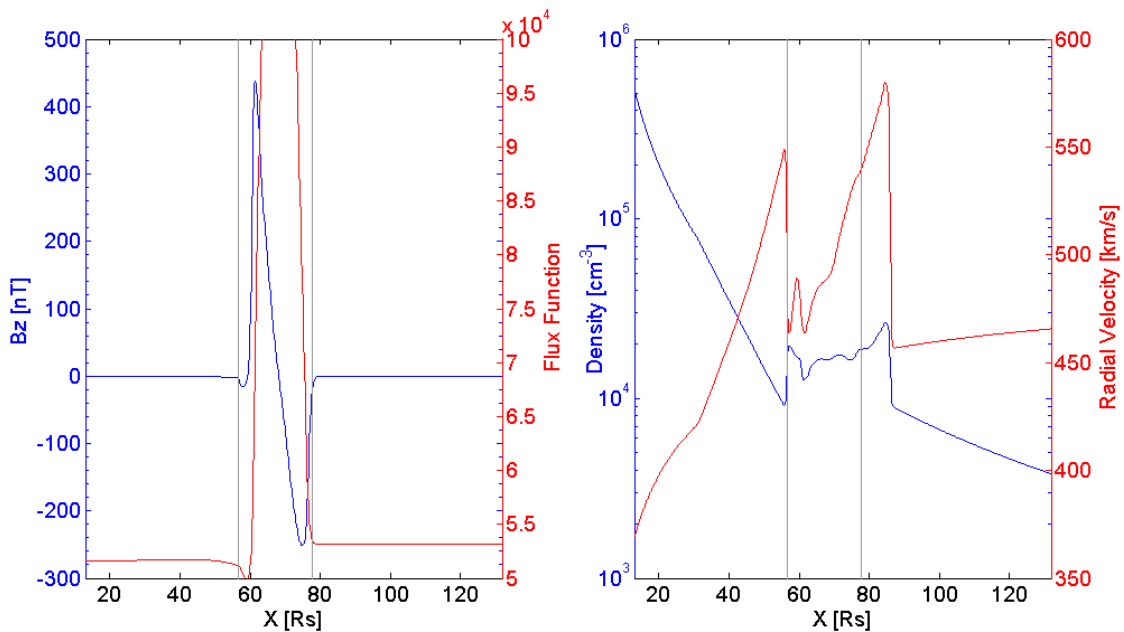
402

403 With the aid of Figure 6, we show that this is the reverse shock pressing onto the solar wind from rear
 404 edge of the CME. This is an effect from introducing a FR with an instantaneous fast speed. The effect can
 405 also be seen in figure 2b, between 3.5 and 10 hours, where a forward-reverse wave pair is initially formed
 406 ahead of the FR; the reverse wave then propagates through the FR resulting in a difference in speed
 407 between the front and rear edge which effectively creates a large expansion velocity for the FR. In the
 408 reference frame of the FR, this causes the rear edge of the FR to ram into the background solar wind
 409 causing a forward- reverse pair of shocks. This type forward-reverse pair behaviour has also been noted
 410 as an ‘over-expansion’ of a CME (Gosling et al. 1995) and occurred in uniform solar wind conditions
 411 such as our simulation; however the observations occurred at high latitudes within fast solar wind
 412 conditions. Therefore, although the global properties after ~ 0.5 AU appear similar to those observed by
 413 Gosling et al. (1995), we believe the reasons for the forward-reverse pair are different in our simulation.
 414 This behaviour of a shock wave travelling through the CME at an early stage of its propagation (i.e.
 415 $\lesssim 30R_s$) when the CME has a mostly circular cross-section may account for the slightly different magnetic
 416 structure to that simulated by Riley & Crooker (2004). In our simulations the shape of the flux rope is
 417 slightly unusual in that its lateral expansion appears to only involve the outer most flux (shown by the

418 single most extended field line) which expands to maintain the nearly constant angular width (50°) of the
 419 flux rope. This small amount of flux forms a thin ‘wing’ while the majority of the flux remains nearly
 420 circular in shape rather than being evenly distorted into an oblate shape. These wings have a higher
 421 plasma beta value (greater than 1) than the central sections of the FR – see figure 4. Further investigation
 422 into this behaviour would require more detailed studies in varying the initial speeds and by incorporating a
 423 more realistic acceleration process during the injection of the CME. These extended wings also appear to
 424 trigger strong inflows behind the flux rope. This can be clearly seen in figure 3b and figure 4 with the
 425 vector arrows of the flow direction. The previously open field lines of the solar wind are drawn into a
 426 deep u-shape behind the rear edge at two locations adjacent to the wings and reconnect to form closed
 427 flux systems.

428

429 The location of the FR is shown between two vertical grey lines in the right hand panel of Figure 6.
 430 Figure 6 displays the result of a 1D spatial cut through the ecliptic. Therefore in this figure, we display the
 431 forward shock to the right (i.e. at a larger heliocentric distance) of the reverse shock (indicated by large
 432 discontinuities in the velocity profile), whereas it is often observed the other way for a time series of in
 433 situ measurements. We choose to display our figure this way because we do not focus on the specific
 434 nature of the forward-reverse pair, but instead are interested in the spatial locations of the FR and its
 435 associated forward shock front ahead.

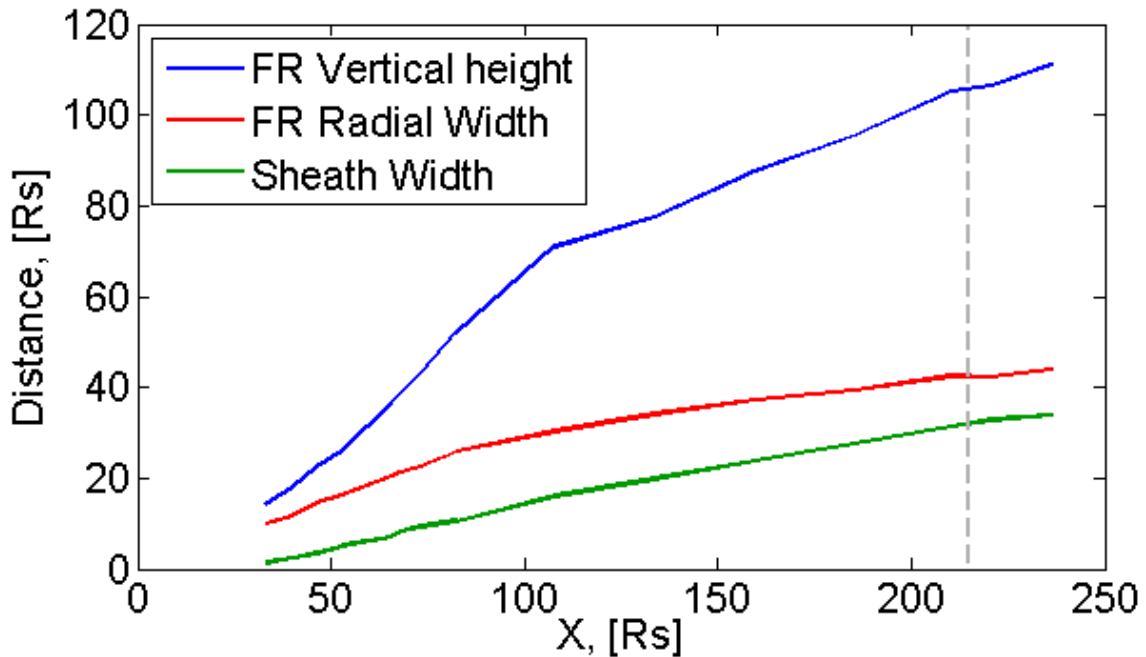


436

437 Figure 6. A 1D cut of the simulated domain from Case 1, when the FR is located at approximately 70Rs.
 438 The spatial profile was taken along the ecliptic. The left panel displays the magnetic field component (B_z ,
 439 blue) that is perpendicular to the ecliptic plane and the flux function (red). Right panel: shows the density
 440 of the solar wind plasma (blue) and the radial component of the velocity (red).

441
442
443
444
445
446
447
448
449
450
451
452
453
454
455
456
457

The heliocentric position of the shock and the flux rope boundary were manually selected within fixed frames. For the four simulations, between 15 and 20 frames were selected, and the flux rope boundary was defined by four points: two along the ecliptic which measured the radial width of the flux rope by inspecting the flux function in figure 6; and two perpendicular to the radial which measures the vertical height (Chen, et al. 1997; Nieves-Chinchilla et al. 2012; Savani et al. 2012), which were estimated from frames similar to figure 2. Figure 7 tracks the increase in the flux rope’s radial width, the perpendicular vertical height and the radial width of the sheath (the shock standoff distance). The vertical height and the sheath width can be clearly seen to increase in size at a faster rate than the radial width of the flux rope; however this is more prominent with the vertical size than the sheath distance. The small increase in the sheath distance relative to the radial width was also observed by Manchester, et al. (2005), and can be qualitatively explained by two potential factors: 1. As the flux rope propagates, it decelerates and thereby decreases the shock strength. So, as the flux rope moves through the heliosphere, the Mach number decreases and the shock standoff distance increases. 2. The morphology of the flux rope changes therefore the dynamics of the standoff distance changes.

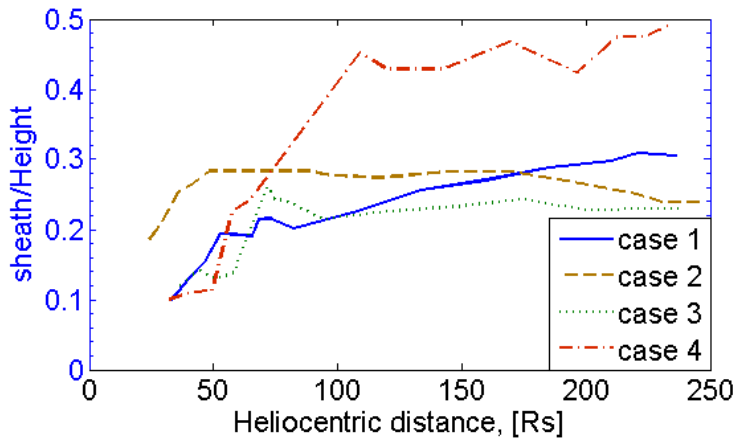


458
459
460
461
462

Figure 7. An investigation of Case 1. The growth of a FR by tracking the increase in the radial width (red), vertical height perpendicular to the radial (blue) and the shock standoff distance (green). The vertical grey dashed line plots the heliocentric distance of Earth.

463
464
465
466
467
468
469
470
471
472
473
474
475
476
477

An analytical investigation of the sheath width (shock standoff distance) normalized to the radius of curvature of the leading edge was carried out by (Siscoe & Odstrcil 2008) with a focus on high Mach number ($M > 5$) conditions. We approximate the radius of curvature to the vertical height of the flux rope in our study and display the results as a function of heliocentric distance in figure 8. Siscoe and Odstrcil investigated the behaviour of the two types of sheath regions for ICMEs and magnetospheres, labelled ‘propagation sheath’ and ‘expansion sheath’, respectively. They conclude that, depending on the fraction of the weighted average between them, the weighted average normalized standoff distance should lie between 0.07 and 0.2. Figure 8 shows that cases 1-3 behave similarly, while case 4 is slightly large. The large expansion and high Mach number during the early propagation phase generates a normalized distance of ~ 0.1 . As the bulk flow of the flux rope decelerates, the Mach number drops; this behaviour along with the possibility that a larger weighting for the ‘propagation sheath’ should be included at the later stages of a CME’s propagation might explain the growing normalized distance towards 0.3. These results are consistent with simulations carried out in the low corona below six solar radii (Loesch et al. 2011).



478
479
480
481
482
483
484
485
486
487

Figure8. An investigation of cases 1-4. The shock standoff distance is normalized to the vertical height of the flux rope (which is used as a proxy to the radius of curvature).

Figure 9 displays the ratio of plasma density across the shock front for the four simulations investigated in this study. The shock jump compression ratio (red dashed line) can be considered as a good proxy for the shock strength (see equation 3 and 4), and is shown to decrease in a non-linear way as the flux rope propagates into the heliosphere. However, we should note that the flux rope and the plasma parameters are not investigated until $\sim 25Rs$. This is because the flux rope is unrealistically initiated much further into

488 the heliosphere than is observed and the sudden acceleration of the flux rope in the early phase would not
489 be considered as typical propagation. The panels a – d represent the calculated parameters for case 1 –4
490 respectively. In this study we investigate the DR coefficient, k_{dr} , by re-arranging equation 1. This enables
491 us to avoid the complications that arise from using different specific heat ratios or from using the
492 mathematical derivations of Mach number from HD or MHD (equation 3 and 4). In addition, equation 1
493 is not explicitly related to the vertical height of the FR. As we wish to capture the behaviour of the shock
494 and the appropriate jump conditions the specific heat ratio, γ , is set to 1.4. This is slightly below the 5/3
495 value of a thermodynamic monatomic ideal gas, therefore the theoretical maximum compression ratio is 6
496 and not 4 in our simulation. This is evident when inspecting the early stages of propagation for Case 4
497 (panel d), where the plasma compression ratio peaks to a little over 5.

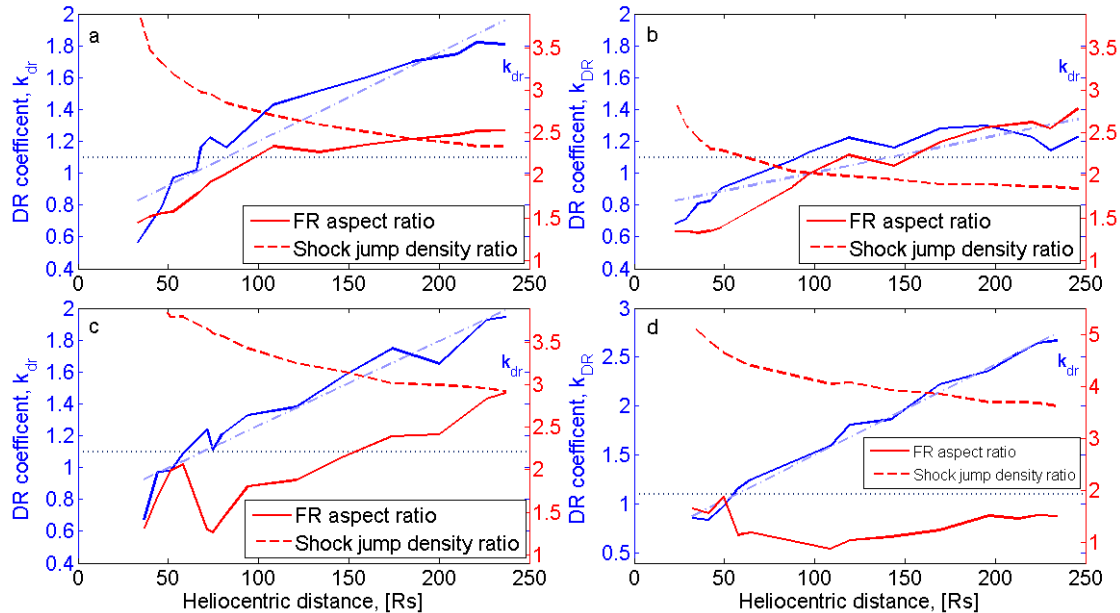
498
499 The DR coefficient (blue solid line) in figure 9 shows a clear dependence on heliocentric distance. The
500 popular value of 1.1 from equation 1, recently used to investigate in situ studies of CMEs (Savani, et al.
501 2011b) and remote observations (Gopalswamy, et al. 2012), is displayed as a horizontal dotted grey line.
502 The lower bound appears to be consistent for all the simulations and remains approximately 0.8 ± 0.1 at
503 small heliocentric distances. This value supports equation 2 and the spherical geometry of a
504 magnetosphere studied by Seiff (1962) from the Sun to a heliocentric distance of about 30Rs (~ 0.15 AU).
505 k_{dr} appears to increase linearly with heliocentric distance as can be seen by the linear best fit curve
506 displayed as a blue dot-dashed line. The linear approximation appears to improve as the initial speed of
507 the injected CME increases. We hypothesize that the change in k_{dr} is due to the change in the CME shape,
508 which becomes more oblate as it propagates (indicated by the increase in aspect ratio). Panel d appears to
509 contradict this hypothesis, by showing an aspect ratio that remains predominately constant at a little above
510 1. However, caution should be taken when considering panel d because the large injected speed of the
511 CME (1200km/s) is a limitation on our simulation. The effect of this large speed on our simulation is to
512 dramatically increase the radial expansion of the CME, which is perhaps not entirely realistic to
513 observations even though evidence of many CMEs with small aspect ratios have been made (Lynnyk, et
514 al. 2011; Savani, et al. 2011b). So the linear increase in k_{dr} is more accurately linked, not to the aspect
515 ratio, but to the size and the radius of curvature of the CME's leading edge.

516
517 Panel a, b, and c have been set to the same x/y axes for the ease of comparing k_{dr} for the different
518 simulations. Panel a and c show that an increase in speed which increases the density compression ratio
519 across the shock and the aspect ratio of the CME has little effect on k_{dr} (k_{dr} is about 1.8 ± 0.3 at Earth for
520 both simulations). These two simulations also show that the coefficient remains predominately above the
521 nominal 1.1 during the CME's propagation to 250Rs, achieving $k_{dr}=1.1$ at approximately 80Rs.

522
 523
 524
 525
 526
 527
 528
 529
 530
 531
 532
 533
 534
 535
 536
 537
 538

Case 2 (Panel b) displays the results for an initial flux rope with half the diameter, and hence half the angular width, of case 1 (panel a). Here we see a significant difference between the k_{dr} values even though the aspect ratio of both CME's appear to be similar. This means the difference is due to the vertical extent of the CME, which supports our early suggestion that the radius of curvature (vertical extent) of the flux rope's leading edge is a significant variable that changes k_{dr} . Case 2 shows that for smaller CMEs with an angular width of $\sim 22.6^\circ$, a k_{dr} value of 1.1 appears to be adequate between the Sun and 215Rs as a first approximation because the value only varies between 0.8 and 1.25.

Finally, our results are in good agreement with density ratios derived by remote observations of CME-driven shocks at heights below 20Rs (Ontiveros & Vourlidas 2009). They obtained density compression ratios of >1.5 for distances above 12 Rs. If we combine the Ontiveros and Vourlidas (2009) measurements with our results, we conclude that the density compression ratio should increase up to a height of about 20-30Rs and then begin to decrease. This implies that CMEs tend to decelerate above 30Rs. Further remote measurements of density compression ratios, especially in the fields of view of heliospheric imagers (>40 Rs), will be highly valuable in verifying our simulation results.



539
 540
 541
 542
 543
 544

Figure 9. The aspect ratio (red solid line), plasma density compression ratio across the shock (red dashed line) and the DR coefficient (blue solid line) from equation 1 are displayed as a function of heliocentric distance, X . The blue and red curves relate to the left and right vertical y-axis, respectively. The linear best fit for k_{dr} is displayed as a dot-dashed blue line, while the expect value is the grey dotted line at 1.1. Panels a, b, c and d correspond to case 1, 2, 3 and 4, respectively.

545

546 5. Conclusions

547

548 In this paper we investigate the behaviour of a CME and its associated shock standoff distance with the
549 aid of 2.5D simulations between 10 and 300 Rs. By examining the density compression ratio coefficient,
550 k_{dr} (from equation 1), we investigate the appropriateness of comparing the geometry of Earth's
551 magnetosheath to a sheath found downstream of a CME-associated shock. We have chosen to investigate
552 this problem with 2.5D simulations rather than the 3D case for reasons of computational speed, our ability
553 to simply repeat the problem for different initial parameters and because the scientific study concentrates
554 only on the cross-sectional cut through the axis of a flux rope. However, we note a comparison between
555 2.5D and 3D simulations have been made (Jacobs, et al. 2007), and have concluded that the results are
556 similar when their injected radial momenta are the same.

557

558 We conclude that a comparison between Earth Magnetosphere and a magnetic flux rope like structure, as
559 expressed in equation 1, is appropriate as a first approximation, in particular for narrow CMEs. But also,
560 that the geometry of a CME changes during its propagation and therefore the k_{dr} value changes. It is more
561 appropriate to use a k_{dr} value of 0.8 ± 0.1 for small heliocentric distances (i.e. for remote observations
562 between 1 and 30Rs). This lower k_{dr} value corresponds to an estimated spherical geometry of Earth's
563 magnetosphere (equation 2, Seiff 1962). This geometry and a value of 0.8 was shown to be successful at
564 estimating the magnetic field strength in the corona where the CME was observed and measured as a
565 circular structure (Kim et al. 2012). As the CME propagates the cross section becomes more oblate and
566 the k_{dr} value increases linearly with heliocentric distance, such that $k_{dr} = 1.1$ is most appropriate at a
567 heliocentric distance of about 80Rs. For terrestrial distances (215Rs) we estimate $k_{dr} = 1.8 \pm 0.3$, which
568 also indicates that the CME structure is generally more oblate than Earth's magnetosphere.

569

570 In the four simulated case studies, we investigated the effect of initial speed and the size of the injected
571 flux rope. We can see that the k_{dr} value is significantly affected by the CME's heliocentric distance and by
572 the size (radius of curvature) of the leading edge of the magnetic flux rope. The initial speed appears to
573 have only a small effect, with the exception of case 4, which may reflect a limitation of our model,
574 namely due to excessive radial expansion created from an instantaneous initial flux rope speed. However,
575 as the initial speed of the flux rope was increased the uncertainty in the linear best fit curve for k_{dr} values
576 (as a function of distance) decreased. The magnetic field strength within the flux rope (between case 1
577 and 2) also had a less significant effect.

578

579 Throughout the analysis, we have concentrated on the height of the CME as a proxy for the radius of
580 curvature of the leading edge in the plane of the cross section. Realistic CMEs are 3D objects that also
581 possess a curvature of the leading edge that is perpendicular to the cross section. We have chosen to
582 ignore this effect here. In essence, we have assumed that the radius of curvature in this dimension is
583 significantly larger than the cross section curvature, which we can therefore assume to be linear. As our
584 simulation is 2.5D, our propagating flux rope is in fact a 3D torus whose perpendicular curvature is the
585 same as the heliocentric distance.

586
587 This work also concentrated on the radial width of a CME along the center of the flux rope. It is
588 extremely unlikely that any spacecraft would travel exactly through the center, and therefore our analysis
589 is idealised. Also for the simplicity of measuring the aspect ratio of the flux rope at specified frames, we
590 did not measure the radial width of the CME as a time series. Due to a flux rope expanding while it passes
591 over a fixed position, a difference of approximately 5% is expected between the radial widths of the two
592 different methods (Owens, et al. 2006). Our method is therefore less appropriate for any comparison to in
593 situ measurements but more relevant to the underlying physics for k_{dr} values. Also recent observations
594 (Nieves-Chinchilla, et al. 2012; Vourlidas et al. 2011) and simulations (Shiota, et al. 2010) have shown
595 that CMEs may rotate as they propagate; this would also complicate any attempt to estimate the aspect
596 ratio from in situ measurements.

597
598 Any future investigation should try to mitigate the limitations of our work by focusing on the flux rope
599 structure at smaller heliocentric distances ($<30R_s$), so that more detailed comparisons can be made for
600 remotely observed CMEs (Gopalswamy, et al. 2012). Also, an improvement on our instantaneous
601 injection of a fast flux rope can be made by introducing a flux rope with a more realistic acceleration over
602 a short distance. This will allow future work to study larger maximum speeds and therefore investigate
603 extreme events that are more likely to be significantly geo-disruptive.

604
605
606

607 **Acknowledgments.** NPS was supported by the NASA Living With a Star Jack Eddy Postdoctoral
608 Fellowship Program, administered by the UCAR Visiting Scientist Programs and hosted by the Naval
609 Research Laboratory. NPS and AV were supported by NASA and the office of Naval Research. The
610 numerical calculations were made using the supercomputing cluster at the Solar Terrestrial Environment
611 laboratory, Nagoya University.

Reference

- 612
613
614 Antiochos, S. K., DeVore, C. R., & Klimchuk, J. A. 1999, *ApJ*, 510(1), 485-493, doi:
615 10.1086/306563
- 616 Burlaga, L., Sittler, E., Mariani, F., & Schwenn, R. 1981, *Journal of Geophysical Research-*
617 *Space Physics*, 86(NA8), 6673-6684, doi: 10.1029/JA086iA08p06673
- 618 Burlaga, L. F. 1988, *Journal of Geophysical Research-Space Physics*, 93(A7), 7217-7224, doi:
619 10.1029/JA093iA07p07217
- 620 Chen, J. 1989, *ApJ*, 338(1), 453-470, doi: 10.1086/167211
- 621 Chen, J., et al. 1997, *ApJ*, 490(2), L191-&, doi: 10.1086/311029
- 622 Chen, P. F., & Shibata, K. 2000, *ApJ*, 545(1), 524-531, doi: 10.1086/317803
- 623 Davies, J. A., et al. 2009, *GeoRL*, 36, doi: 10.1029/2008gl036182
- 624 Dedner, A., Kemm, F., Kroner, D., Munz, C. D., Schnitzer, T., & Wesenberg, M. 2002, *JCoPh*,
625 175(2), 645-673, doi: 10.1006/jcph.2001.6961
- 626 Eyles, C. J., et al. 2009, *SoPh*, 254(2), 387-445, doi: 10.1007/s11207-008-9299-0
- 627 Eyles, C. J., et al. 2003, *SoPh*, 217(2), 319-347, doi: 10.1023/b:sola.0000006903.75671.49
- 628 Fairfield, D. H., Cairns, I. H., Desch, M. D., Szabo, A., Lazarus, A. J., & Aellig, M. R. 2001,
629 *Journal of Geophysical Research-Space Physics*, 106(A11), 25361-25376, doi:
630 10.1029/2000ja000252
- 631 Farris, M. H., & Russell, C. T. 1994, *Journal of Geophysical Research-Space Physics*, 99(A9),
632 17681-17689, doi: 10.1029/94ja01020
- 633 Forbes, T. G., & Priest, E. R. 1995, *ApJ*, 446(1), 377-389, doi: 10.1086/175797
- 634 Gopalswamy, N., Nitta, N., Akiyama, S., Mäkelä, P., & Yashiro, S. 2012, *ApJ*, 744(1), doi:
635 10.1088/0004-637X/744/1/72
- 636 Gopalswamy, N., & Yashiro, S. 2011, *Astrophysical Journal Letters*, 736(1), doi: 10.1088/2041-
637 8205/736/1/117
- 638 Gopalswamy, N., Yashiro, S., Michalek, G., Stenborg, G., Vourlidas, A., Freeland, S., &
639 Howard, R. 2009, *EM&P*, 104(1-4), 295-313, doi: 10.1007/s11038-008-9282-7
- 640 Gosling, J. T., McComas, D. J., Phillips, J. L., Pizzo, V. J., Goldstein, B. E., Forsyth, R. J., &
641 Lepping, R. P. 1995, A CME-driven solar wind disturbance observed at both low and high
642 heliographic latitudes, *Geophys. Res. Lett.*, 22 (13), 1753 – 1756, doi:10.1029/95GL01776

- 643 Hidalgo, M. A., Cid, C., Vinas, A. F., & Sequeiros, J. 2002, *Journal of Geophysical Research-*
644 *Space Physics*, 107(A1), doi: 10.1029/2001ja900100
- 645 Howard, R. A., Michels, D. J., Sheeley, N. R., & Koomen, M. J. 1982, *ApJ*, 263(2), L101-&
646 doi: 10.1086/183932
- 647 Inoue, S., & Kusano, K. 2006, *ApJ*, 645(1), 742-756, doi: 10.1086/503153
- 648 Jackson, B. V., et al. 2004, *SoPh*, 225(1), 177-207, doi: 10.1007/s11207-004-2766-3
- 649 Jacobs, C., van der Holst, B., & Poedts, S. 2007, *Astronomy & Astrophysics*, 470(1), 359-365,
650 doi: 10.1051/0004-6361:20077305
- 651 Kaiser, M. L., Kucera, T. A., Davila, J. M., Cyr, O. C. S., Guhathakurta, M., & Christian, E.
652 2008, *SSRv*, 136(1-4), 5-16, doi: 10.1007/s11214-007-9277-0
- 653 Kartalev, M., Dryer, M., Grigorov, K., & Stoimenova, E. 2006, *Journal of Geophysical*
654 *Research-Space Physics*, 111(A10), doi: 10.1029/2006ja011760
- 655 Kataoka, R., Ebisuzaki, T., Kusano, K., Shiota, D., Inoue, S., Yamamoto, T. T., & Tokumaru, M.
656 2009, *Journal of Geophysical Research-Space Physics*, 114, doi: 10.1029/2009ja014167
- 657 Kim, R.-S., Gopalswamy, N., Moon, Y.-J., Cho, K.-S., & Yashiro, S. 2012, *Astrophysical*
658 *Journal Letters*, 746(2), 118, doi: 10.1088/0004-637X/746/2/118
- 659 Krall, J., Chen, J., Duffin, R. T., Howard, R. A., & Thompson, B. J. 2001, *ApJ*, 562(2), 1045-
660 1057, doi: 10.1086/323844
- 661 Kusano, K., Maeshiro, T., Yokoyama, T., & Sakurai, T. 2004, *ApJ*, 610(1), 537-549, doi:
662 10.1086/421547
- 663 Lepping, R. P., Jones, J. A., & Burlaga, L. F. 1990, *Journal of Geophysical Research-Space*
664 *Physics*, 95(A8), 11957-11965, doi: 10.1029/JA095iA08p11957
- 665 Linker, J. A., et al. 1999, *Journal of Geophysical Research-Space Physics*, 104(A5), 9809-9830,
666 doi: 10.1029/1998ja900159
- 667 Lockwood, M., Forsyth, R. B., Balogh, A., & McComas, D. J. 2004, *AnGeo*, 22(4), 1395-1405,
668 doi: 10.5194/angeo-22-1395-2004
- 669 Loesch, C., Opher, M., Alves, M. V., Evans, R. M., & Manchester, W. B. 2011, *Journal of*
670 *Geophysical Research-Space Physics*, 116, doi: 10.1029/2010ja015582
- 671 Lugaz, N., Manchester, W. B., & Gombosi, T. I. 2005, *ApJ*, 627(2), 1019-1030, doi:
672 10.1086/430465
- 673 Lynnyk, A., Safrankova, J., Nemecek, Z., & Richardson, J. D. 2011, *P&SS*, 59(9), 840-847, doi:
674 10.1016/j.pss.2011.03.016

- 675 Maloney, S. A., & Gallagher, P. T. 2011, *Astrophysical Journal Letters*, 736(1), L5, doi:
676 10.1088/2041-8205/736/1/15
- 677 Manchester, W. B., et al. 2005, *ApJ*, 622(2), 1225-1239, doi: 10.1086/427768
- 678 Manchester, W. B., et al. 2004, *Journal of Geophysical Research-Space Physics*, 109(A1), doi:
679 10.1029/2002ja009672
- 680 Manchester, W. B., Ridley, A. J., Gombosi, T. I., & DeZeeuw, D. L. 2006, *AdSpR*, 38(2), 253-
681 262, doi: 10.1016/j.asr.2005.09.044
- 682 Marubashi, K. 1986, *AdSpR*, 6(6), 4, doi: 10.1016/0273-1177(86)90172-9
- 683 Miller, G., & Turner, L. 1981, *PhFl*, 24(2), 363-365, doi: 10.1063/1.863351
- 684 Miyoshi, T., & Kusano, K. 2005, *JCoPh*, 208(1), 315-344, doi: 10.1016/j.jcp.2005.02.017
- 685 Mulligan, T., & Russell, C. T. 2001, *Journal of Geophysical Research-Space Physics*, 106(A6),
686 10581-10596, doi: 10.1029/2000ja900170
- 687 Nieves-Chinchilla, T., et al. 2012, *Journal of Geophysical Research-Space Physics*, In Press,
- 688 Ontiveros, V., & Vourlidas, A. 2009, *ApJ*, 693(1), 267-275, doi: 10.1088/0004-637x/693/1/267
- 689 Owens, M. J., & Crooker, N. U. 2006, *Journal of Geophysical Research-Space Physics*,
690 111(A10), doi: 10.1029/2006ja011641
- 691 Owens, M. J., Merkin, V. G., & Riley, P. 2006, *Journal of Geophysical Research-Space Physics*,
692 111(A3), doi: 10.1029/2005ja011460
- 693 Pomoell, J., & Vainio, R. 2012, *ApJ*, 745(2), doi: 10.1088/0004-637x/745/2/151
- 694 Pomoell, J., Vainio, R., & kissmann, R. 2011, *ASTRA*, 7(3), 387-394, doi: 10.5194/astra-7-387-
695 2011
- 696 Press, W. H.; Flannery, B. P.; Teukolsky, S. A.; and Vetterling, W. T. 1992, *Successive*
697 *Overrelaxation (SOR), Numerical Recipes in FORTRAN: The Art of Scientific Computing*, 2nd
698 ed. (Cambridge University Press), 866-869
- 699 Priest, E., & Forbes, T. 2007, *Magnetic Reconnection: MHD Theory and Applications*
700 (Cambridge University Press)
- 701 Priest, E. R. 1984, *Solar magneto-hydrodynamics* (D. Reidel Pub. Co.)
- 702 Riley, P., & Crooker, N. U. 2004, *ApJ*, 600(2), 1035-1042, doi: 10.1086/379974
- 703 Rouillard, A. P., et al. 2009, *SoPh*, 256(1-2), 307-326, doi: 10.1007/s11207-009-9329-6
- 704 Roussev, I. I., Lugaz, N., & Sokolov, I. V. 2007, *ApJ*, 668(1), L87-L90, doi: 10.1086/522588

705 Russell, C. T., & Mulligan, T. 2002, P&SS, 50(5-6), 527-534, doi: 10.1016/s0032-
706 0633(02)00031-4

707 Savani, N. P., et al. 2012, SoPh, 279(2), 517-535, doi: 10.1007/s11207-012-0041-6,

708 Savani, N. P., Owens, M. J., Rouillard, A. P., Forsyth, R. J., Kusano, K., Shiota, D., & Kataoka,
709 R. 2011a, ApJ, 731(2), doi: 10.1088/0004-637x/731/2/109

710 Savani, N. P., et al. 2011b, ApJ, 732(2), doi: 10.1088/0004-637x/732/2/117

711 Savani, N. P., Rouillard, A. P., Davies, J. A., Owens, M. J., Forsyth, R. J., Davis, C. J., &
712 Harrison, R. A. 2009, AnGeo, 27(11), 4349-4358, doi: 10.5194/angeo-27-4349-2009

713 Seiff, A. 1962, in Gas dynamics in space exploration, 269 - 282

714 Sheeley, N. R., Walters, J. H., Wang, Y. M., & Howard, R. A. 1999, Journal of Geophysical
715 Research-Space Physics, 104(A11), 24739-24767, doi: 10.1029/1999ja900308

716 Shiota, D., Isobe, H., Chen, P. F., Yamamoto, T. T., Sakajiri, T., & Shibata, K. 2005, ApJ,
717 634(1), 663-678, doi: 10.1086/496943

718 Shiota, D., Kusano, K., Miyoshi, T., Nishikawa, N., & Shibata, K. 2008, Journal of Geophysical
719 Research-Space Physics, 113(A3), doi: 10.1029/2007ja012516

720 Shiota, D., Kusano, K., Miyoshi, T., & Shibata, K. 2010, ApJ, 718(2), 1305-1314, doi:
721 10.1088/0004-637x/718/2/1305

722 Siscoe, G., & Odstroil, D. 2008, Journal of Geophysical Research-Space Physics, 113, doi:
723 10.1029/2008ja013142

724 Spreiter, J. R., Summers, A. L., & Alksne, A. Y. 1966, P&SS, 14(3), 223-&, doi: 10.1016/0032-
725 0633(66)90124-3

726 St Cyr, O. C., et al. 2000, Journal of Geophysical Research-Space Physics, 105(A8), 18169-
727 18185, doi: 10.1029/1999ja000381

728 Titov, V. S., & Demoulin, P. 1999, A&A, 351(2), 707-720,

729 Totten, T. L., Freeman, J. W., & Arya, S. 1995, Journal of Geophysical Research-Space Physics,
730 100(A1), 13-17, doi: 10.1029/94ja02420

731 Tsurutani, B., Wu, S. T., Zhang, T. X., & Dryer, M. 2003, Astronomy & Astrophysics, 412(1),
732 293-304, doi: 10.1051/0004-6361:20031413

733 Verigin, M., et al. 2003, Journal of Geophysical Research-Space Physics, 108(A8), doi:
734 10.1029/2002ja009711

735 Vourlidas, A., Colaninno, R., Nieves-Chinchilla, T., & Stenborg, G. 2011, Astrophysical Journal
736 Letters, 733(2), doi: 10.1088/2041-8205/733/2/l23

737 Vourlidas, A., Howard, R. A., Esfandiari, E., Patsourakos, S., Yashiro, S., & Michalek, G. 2010,
738 ApJ, 722(2), 1522-1538, doi: 10.1088/0004-637x/722/2/1522

739 Yashiro, S., Gopalswamy, N., Michalek, G., St Cyr, O. C., Plunkett, S. P., Rich, N. B., &
740 Howard, R. A. 2004, Journal of Geophysical Research-Space Physics, 109(A7), doi:
741 10.1029/2003ja010282
742
743
744